Three-dimensional reconstruction of granular porous media based on deep generative models

Rongyan Yin, Qizhi Teng,* Xiaohong Wu, Fan Zhang, and Shuhua Xiong
College of Electronics and Information Engineering, Sichuan University, Chengdu 610065, China

(Received 24 May 2023; accepted 9 October 2023; published 9 November 2023)

Reconstruction of microstructure in granular porous media, which can be viewed as granular assemblies, is crucial for studying their characteristics and physical properties in various fields concerned with the behavior of such media, including petroleum geology and computational materials science. In spite of the fact that many existing studies have investigated grain reconstruction, most of them treat grains as simplified individuals for discrete reconstruction, which cannot replicate the complex geometrical shapes and natural interactions between grains. In this work, a hybrid generative model based on a deep-learning algorithm is proposed for high-quality three-dimensional (3D) microstructure reconstruction of granular porous media from a single two-dimensional (2D) slice image. The method extracts 2D prior information from the given image and generates the grain set as a whole. Both a self-attention module and effective pattern loss are introduced in a bid to enhance the reconstruction ability of the model. Samples with grains of varied geometrical shapes are utilized for the validation of our method, and experimental results demonstrate that our proposed approach can accurately reproduce the complex morphology and spatial distribution of grains without any artificiality. Furthermore, once the model training is complete, rapid end-to-end generation of diverse 3D realizations from a single 2D image can be achieved.

DOI: 10.1103/PhysRevE.108.055303

I. INTRODUCTION

Granular porous media, featuring packing of grains varying in shape and size, play an assignable role in many engineering applications, petroleum geology, and computational material science in particular [1,2]. Experimental investigations have implied that granule morphological features have great impacts on the physical performance of granular porous materials, including permeability, elasticity, etc. [3–8]. Fast and accurate establishment of structural models has been the subject of intensive studies further investigating the physical behavior of granular porous media.

Currently, there are two main methods for the acquisition of the microstructure of granular porous media: digital imaging technologies and numerical simulation algorithms. Just as the name implies, digital imaging methods utilize advanced imaging devices to visually display the three-dimensional morphological characteristics, which include x-ray computed tomography (CT) scanning [9–11], focused ion beam–scanning electron microscopy (FIB-SEM) [12–14], and other techniques. Despite the significant improvement in the accuracy of instruments, the contradiction between the field of view and resolution remains a Gordian knot, in addition to the high cost and time-intensive efforts required.

It is, however, inescapable that costly and time-consuming physical experiments based on real samples are insufficient in many fields in which accurate analyses of the properties require a large number of representative samples. With the objective being to avoid a long collection process, numerical reconstructions of granular porous materials have garnered considerable attention in the search for stochastic models whose grain distribution and characteristics approximate real conditions to improve our understanding of the macrophysical properties. Numerical simulation methods can be divided into four kinds, i.e., process-based reconstruction methods [15–17], object-based methods [18–23], statistical methods [24–32], and deep-learning-based methods [33–38].

Process-based reconstruction methods tend to be mature following decades of development and can build more realistic models because fundamental concepts of natural formation processes of materials can be mimicked, including grain sedimentation and compaction and diagenetic rock transformations [15–17]. Although they are favorable, these methods are restrained to application scenarios in which grains fuse together in a certain simple manner and have the unrealistic assumption that all grains are of regular shapes. Additionally, such methods are computationally intensive and require extensive calibration to define separate rules for each type of core with different formation processes.

Another widely used reconstruction approach for granular porous media is object-based methods in which grains that make up the materials are considered to be individual objects regardless of how they formed. In granular porous media known as solid grain assemblies, the state would be changed by a supply of external energy, which may cause the grains to behave like a fluid [39]. The discrete element method (DEM) is capable of characterizing the evolution of some grain-scale quantities in granular porous media, facilitating the understanding of bulk behaviors of interest. Therefore, the DEM has become a mainstream method for studying the transport and mechanical properties of these media [18–20]. However, the major drawback of the DEM is the potential for inaccurate simulation results attributed to simplification

*qzteng@scu.edu.cn

 ©2023 American Physical Society

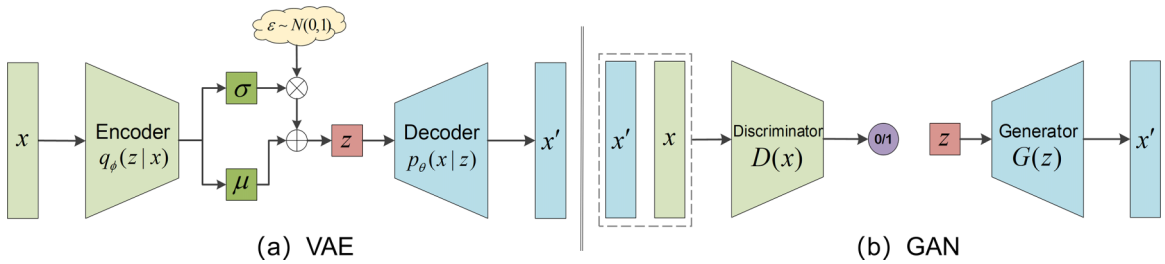

FIG. 1. Schematic description of (a) the VAE and (b) the GAN.

of complexly shaped grains to relatively common regular objects, e.g., ellipsoids and spheroids. Although some research has been dedicated to the utilization of irregularly shaped grains [21–23], the capacity to reproduce realistic granules is still limited when confronted by complicated geometries. In addition, the number of simulated grains is restricted by the computationally intensive nature of the DEM.

Statistical methods [24,25] are those that resort to functional information, which can include statistical or morphological features extracted from images with the intention of recreating structures and distributions of interest. The simulated annealing method [26–28] and multipoint statistics [29–32] are two representative mainstream approaches that have achieved some impressive results. Despite the fact that these methods can reconstruct a three-dimensional (3D) model based on a single two-dimensional (2D) slice, the time tends to increase exponentially as the size of the model increases.

With the vast development and widespread application of deep-learning technologies, scholars have gradually concentrated on introducing these methods into the reconstruction of granular or porous media. For instance, Mosser *et al.* [33] first utilized volumetric generative adversarial networks to achieve three-dimensional image reconstructions of porous media; then, Huang *et al.* [34] successfully generated granular porous media at the grain scale using STYLEGAN [40]. However, most of these methods concentrate on 3D-to-3D reconstructions which map a latent noise vector to a 3D structure and require a large number of 3D volumetric representations of media, whereas 2D data are more accessible in practice.

In this study, motivated by the emergence of some novel 2D-to-3D reconstruction methods for porous media, we aim to realize accurate and fast reconstruction of 3D structures from a single 2D slice image [35–38]. In light of the strong learning ability of complicatedly distributed data in deep generative models, particularly in the field of image generation, the proposed method is based on two typical models: the variational autoencoder (VAE) [41] and the generative adversarial network (GAN) [42]. This approach can reproduce irregular grains with shapes as close as possible to those found in real samples and generate the grain assembly. Consequently, the reconstruction results can reflect the spatial distribution of real particulate solids and provide approximately accurate basic models for subsequent simulation experiments on physical properties.

The rest of this paper is organized as follows: In Sec. II, the principles of the two deep generative models are briefly described, and then the framework, loss functions, and structure of our approach are introduced in a comprehensive way. Section III lists experimental datasets and the hyperparameter settings of networks and demonstrates the evaluation criteria for reconstructions, following which experimental results and comparisons are presented. Finally, the paper ends with conclusions in Sec. IV.

II. METHODOLOGY

In this section, we present a comprehensive introduction to our proposed reconstruction algorithm for granular porous media based on deep generative models. This includes an overview of the main principles of our method, the design of network architectures, and the loss functions. To provide a better understanding of the motivation behind our approach, a brief introduction to the fundamentals of the two models involved is provided before we delve into the specifics of our method.

A. Variational autoencoder

As a typical generative model, the VAE possesses two parts, the encoder and the decoder. The former is applied to extract features of the input image $\mathbf{x}$ and map the input image $\mathbf{x}$ to a latent vector space $\mathbf{z}$. After that, the latter decodes vector $\mathbf{z}$ back to an image [41]. Figure 1(a) displays the schematic diagram of the VAE.

Normally, the model is grounded on the assumption that the latent space $\mathbf{z}$ obeys the standard normal distribution. The encoder is modeled as a convolutional neural network with the objective of fitting two parameters with normal distribution, namely, the mean and variance, and then determining the probability distribution $q_\phi(\mathbf{z}|\mathbf{x})$ of the input image $\mathbf{x}$ parameterized by ϕ. The decoder can be regarded as a generative network with weight θ that can generate a fake image conforming to the probability distribution $p_\theta(\mathbf{x}|\mathbf{z})$ by using the resampled vector $\mathbf{z}$ as input. The loss function of the VAE, whose purpose is to minimize the reconstruction error and enforce the posterior probability $q_\phi(\mathbf{z}|\mathbf{x})$ to follow the standard normal distribution, is defined as follows:

$$\begin{aligned}\mathcal{L}_{\mathrm{VAE}} &= -\mathbb{E}_{q_\phi(\mathbf{z}|\mathbf{x})}[\log p_\theta(\mathbf{x}|\mathbf{z})] + D_{\mathrm{KL}}[q_\phi(\mathbf{z}|\mathbf{x})||p(\mathbf{z})] \\ &= \mathcal{L}_{\mathrm{like}}^{\mathrm{pixel}} + \mathcal{L}_{\mathrm{prior}},\end{aligned} \tag{1}$$

where D_{KL} is the Kullback-Leibler divergence.

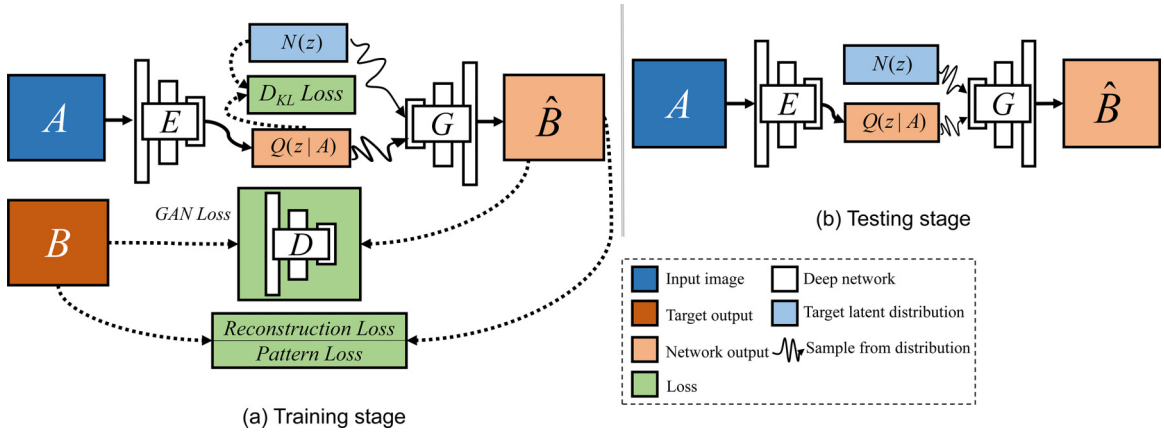

FIG. 2. An overview of our proposed framework. A is the input 2D slice from the target 3D structure B, and $\hat{B}$ is the generated 3D structure.

B. Generative adversarial network

In recent years, because of the strong capability of data generation, GANs have enjoyed immense popularity in the field of computer vision. Unlike the VAE, GANs can generate data that closely approximate real samples from a latent random variable by learning high-dimensional, complex real data distribution without any assumptions about the distribution. The basic architecture of a GAN comprises two significant parts known as the generator G and the discriminator D. The general structure of a GAN can be seen in Fig. 1(b).

In simple terms, the working mechanism of GANs can be described as a zero-sum game between the generator and the discriminator. On the one hand, the generator makes a great effort to reconstruct realistic data that are sufficient to deceive the discriminator. On the other hand, the discriminator gradually develops the ability to distinguish true from false during training, and then the identification result is used as a guide with the intention of improving the generator's production ability. After repeated alternate training, the reconstructed result generated by G closely reproduces the distribution features of real samples so that D cannot distinguish between fake and real samples. Assuming $\mathbf{z}$ is a latent random variance and $\mathbf{x}$ is the real sample, the loss function is defined as

$$\min_G \max_D V(G,D) = \min_G \max_D \mathbb{E}_{\mathbf{x}\sim p_{\text{data}}(\mathbf{x})}[\log D(\mathbf{x})] + \mathbb{E}_{\mathbf{z}\sim p(\mathbf{z})}\{\log[1 - D(G(\mathbf{z}))]\}, \quad (2)$$

where $p_{\text{data}}(\mathbf{x})$ and $p(\mathbf{z})$ denote the probability distribution of the ground truth $\mathbf{x}$ and the noise $\mathbf{z}$, respectively. Equation (2) shows that D tries to maximize $V(G,D)$ by giving high scores to real samples and low scores to fake ones, while G attempts to deceive D by generating samples that can obtain a high score from D. However, it is worth noting that the noise vector $\mathbf{z}$ used as the input for the generator itself does not contain any additional information about the training image.

C. The main idea of our method

In an effort to obtain a performance boost from deep generative models with the respect to reconstruction of granular porous media, our idea is to take full advantage of the VAE and GAN by integrating them into one model. Since a traditional GAN is trained to generate fake images from a noise vector with a random distribution lacking the feature information of the real image, which contributes to the instability and difficulty of the training procedure, we substitute the random noise with a hidden vector in the latent space generated by an encoder in the structure of the VAE.

Given that macroscopic physical properties of materials need a considerable number of samples to be accurately predicted in practical application scenarios, it is of great importance to train a model based on the true original 3D microstructure that can generate 3D synthetic realizations matched with statistical and morphological features directly from 2D image data because 2D images are more accessible than 3D data.

For these reasons, we develop a hybrid model combined with the VAE and GAN whose function is to generate diverse 3D results from a given 2D input image of granular porous media. An overview of our proposed framework is shown in Fig. 2, from which it can be seen that the model comprises three neutral networks: the encoder E, the generator G, and the discriminator D. With the intention of realizing reconstructions from two to three dimensions, we extract the underlying 2D image A of the 3D structure B as input to the encoder, and then complex structure characteristics of the image can be transformed into a latent vector (known as $\mathbf{z}_{\text{enc}}$) following the probability distribution $Q(z|A)$, with which a noise vector (known as $\mathbf{z}_{\text{noise}}$) obeying a Gaussian distribution was concatenated to gain diversity of outputs. As a consequence, the synthesized vector contains the features of the 2D input image, thereby providing prior information for subsequent generator decoding. This ultimately facilitates network training and optimization. Afterwards, the generator attempts to recreate 3D structures from the latent vector as accurately as possible with the assistance of the discriminator. The above-mentioned content is the framework of the training stage since the testing structure can be seen in Fig. 2(b). As our GAN-based model is an end-to-end model, it can learn the feature distribution of 3D training samples adequately enough to quickly obtain more accurate predictions of real 3D structures. More specific network structures will be explained in detail in Sec. II E.

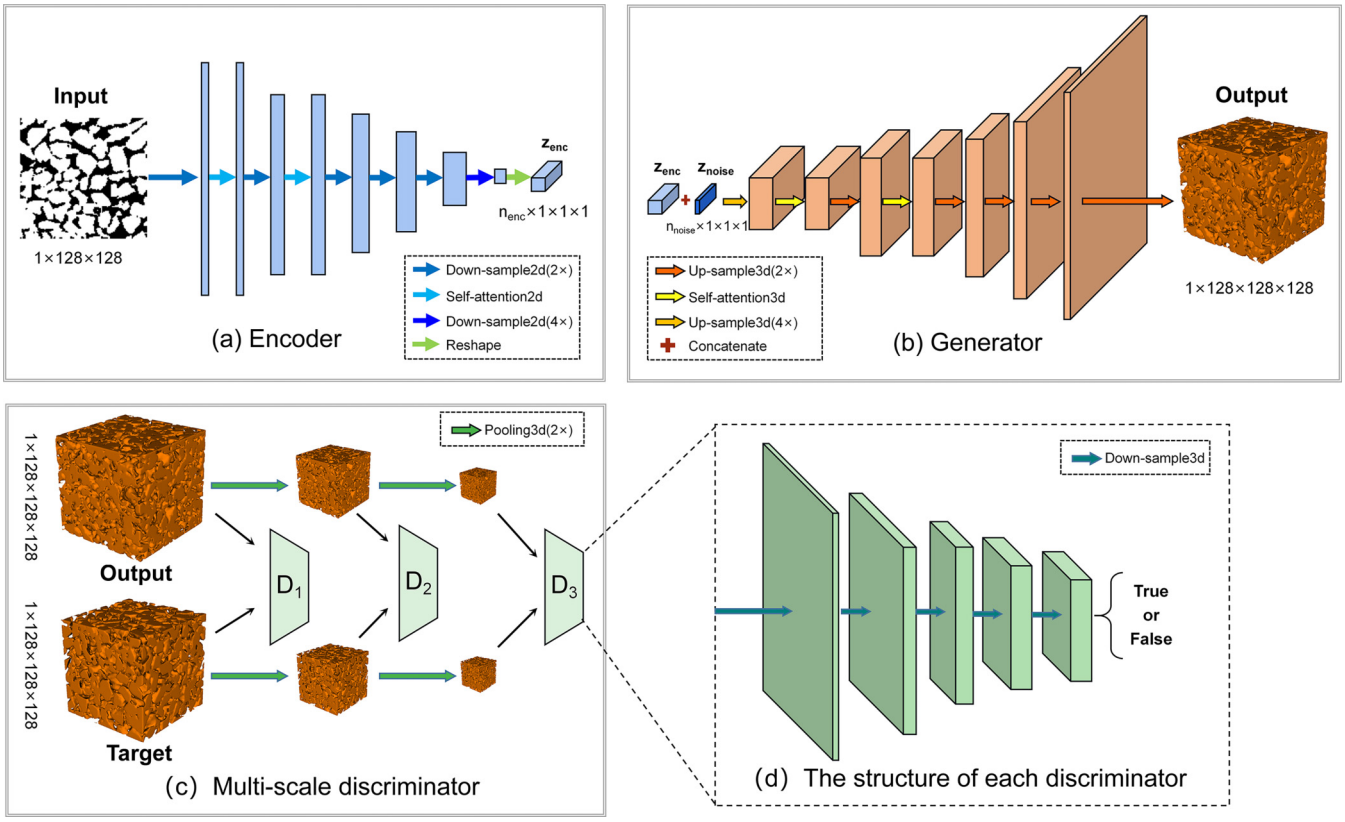

FIG. 3. The architecture of our proposed approach.

D. Loss function

Here, we give detailed information about the loss functions in this study. The standard losses of the VAE and GAN are used. First, the loss of the VAE $\mathcal{L}_{\text{VAE}}$ is given as follows:

$$\mathcal{L}_{\text{VAE}} = \mathcal{L}_{\text{like}}^{\text{pixel}} + \lambda_{kl}\mathcal{L}_{\text{prior}}, \tag{3}$$

where the hyperparameter λ_{kl} controls the proportional weight of the loss $\mathcal{L}_{\text{prior}}$. As Eq. (1) demonstrates, $\mathcal{L}_{\text{like}}^{\text{pixel}}$ represents reconstruction loss, which is employed to calculate the mean square error loss (MSE) between the input 2D image and the first top 2D image of the generated 3D structure; the loss $\mathcal{L}_{\text{prior}}$ serves to evaluate the distance between two distributions, $Q(\mathbf{z}|A)$ and $\mathcal{N} \sim (0, 1)$.

Given the complex and diverse geometrical shapes of grains in granular porous media, we introduce a pattern loss $\mathcal{L}_{\text{pattern}}$ to the loss of G for the purpose of constraining the generator to reconstruct 3D results possessing similar morphological features. This loss [see Eq. (4)] quantifies the MSE of pattern distributions in the correlative images of fake image $G(\mathbf{z}_{\text{enc}}, \mathbf{z}_{\text{noise}})$ and target $\mathbf{y}$. More design details of this loss can be found in Ref. [37]. Since the main object of this paper is the grain rather than the pore, whose size is relatively larger, dilated convolution is chosen to capture the pattern for adequate edge texture information about the granules, and the dilation rate of the convolution is considered as a hyperparameter of the network:

$$\mathcal{L}_{\text{pattern}} = \|\mathbf{y}_{\text{pattern}} - [G(\mathbf{z}_{\text{enc}}, \mathbf{z}_{\text{noise}})_{\text{pattern}}]\|_2^2. \tag{4}$$

The multiscale discriminator used in the model contains three components (denoted D_1, D_2, and D_3), so the loss of the GAN in our framework can be specified as follows:

$$\mathcal{L}_{\text{gan}}^{D} = \frac{1}{3}\sum_{i=1,2,3}\{\mathbb{E}[\log D_i(\mathbf{y}_i)] + \mathbb{E}(\log\{1 - D_i([G(\mathbf{z}_{\text{enc}}, \mathbf{z}_{\text{noise}})]_i)\}), \} \tag{5}$$

$$\mathcal{L}_{\text{gan}}^{G} = \frac{1}{3}\sum_{i=1,2,3}\mathbb{E}(\log\{1 - D_i([G(\mathbf{z}_{\text{enc}}, \mathbf{z}_{\text{noise}})]_i)\}), \tag{6}$$

where $\mathbf{y}_1$ denotes the target 3D image and $\mathbf{y}_2$ and $\mathbf{y}_3$ are images obtained after downsampling the original image once and twice; the same applies to $[G(\mathbf{z}_{\text{enc}}, \mathbf{z}_{\text{noise}})]_i$.

Then, the total loss of the generator is defined as

$$\mathcal{L}_{\text{total}}^{G} = \lambda_{\text{rec}} \times \mathcal{L}_{\text{like}}^{\text{pixel}} + \lambda_{\text{gan}} \times \mathcal{L}_{\text{gan}}^{G} + \lambda_{\text{pattern}} \times \mathcal{L}_{\text{pattern}}, \tag{7}$$

where λ_{rec}, λ_{gan}, and λ_{pattern} are hyperparameters that represent the weight of each loss.

E. Network architectures

In this study, a volumetric version of the deep convolutional generative adversarial network [43] was adopted as the main framework. A module named self-attention was inserted into both the encoder and generator. In the following, we will elaborate on the architectures of the three networks which are illustrated in Fig. 3, as well as the self-attention module.

The encoder is a neural network consisting of a sequence of 2D convolutional layers because it deals with 2D image data, which generally have dimensions of $C \times H \times W$, where C, H, and W signify the channel, height, and width of the

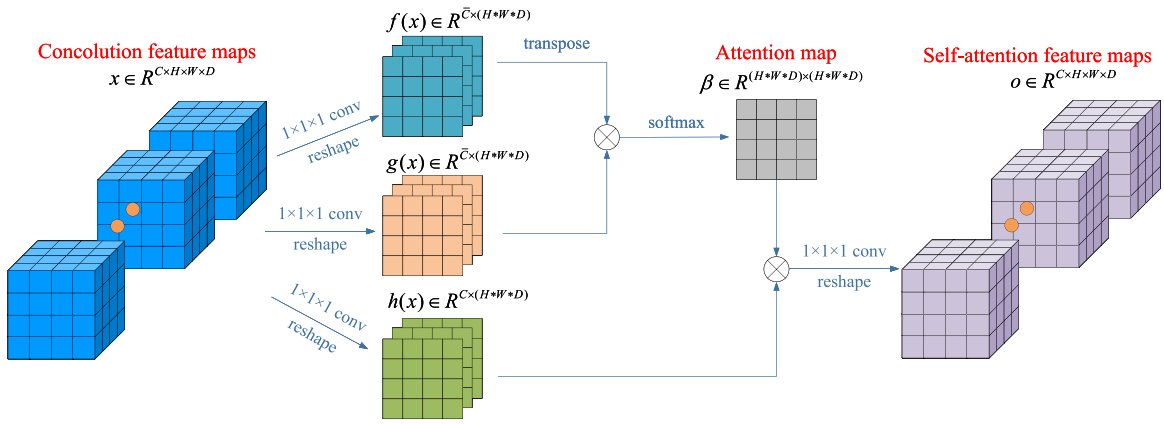

FIG. 4. The 3D self-attention module for the generator in our network. The self-attention module used in the encoder can be obtained by reducing this framework by one dimension.

image, respectively. Encoding may be thought of as gradually increasing the number of channels and downsampling the image. In this approach, as we focus on 128×128 images, the image is transformed into a $128 \times 1 \times 1$ vector. Each convolutional layer is followed by a batch normalization layer and a leaky rectified linear unit activation layer, except the last one, and a 2D version of the self-attention module is inserted after both the first and second convolutional layers.

The purpose of the self-attention module used in our network is to enhance the performance of the encoder and generator, which is represented in Fig. 4. The image feature maps x in the previously hidden layer are transformed into two feature spaces $f(x) = W_f x$ and $g(x) = W_g x$ to calculate attention as in Eq. (8), where β_{ij} represents the degree of participation in the ith location when the network synthesizes the target jth volume,

$$\beta_{j,i} = \frac{\exp(s_{ij})}{\sum_{i=1}^{N} \exp(s_{ij})}, \quad s_{ij} = f\left(x_i^T\right) g(x_j). \tag{8}$$

Subsequently, the third feature space $h(x) = W_h x$ is used to acquire attention feature maps:

$$o_j = v\left(\sum_{i=1}^{N} \beta_{j,i} h(x_i)\right), \; h(x_i) = W_h x_i, \; v(x_i) = W_v x_i. \tag{9}$$

In the above formulations, W_f, W_g, W_h, and W_v are learned weight matrices of $1 \times 1 \times 1$ 3D convolutions. Finally, with a learnable scalar γ initialized as zero, the output of the attention layer is calculated by

$$y_i = \gamma o_i + x_i. \tag{10}$$

With the assistance of self-attention modules, the network is able to capture both long- and short-range dependences and escape the localization limitation of convolution [44].

At the end of the encoding, the output of E is reshaped into three dimensions and combined with a 3D noise vector, after which the synthetic vector is fed into the generator. The structure of G is arguably symmetrical to that of the encoder except for the difference in dimensional space, as the input of G is 3D data. The self-attention module in G depicted in Fig. 4 is applied to make the generated images contain more realistic details. After a series of 3D convolution operations, the synthetic vector is finally decoded into a 3D output which is then sent to the discriminator along with the target structure to determine whether it is true or false.

The discriminator module D in the model is designed as a multiscale discriminator consisting of three discriminators (denoted D_1, D_2, and D_3) with the same architecture but different weights. Training samples the size of the original are fed into D_1, and the inputs of D_2 and D_3 are downsampled two and four times from the original size, respectively. The multiscale discriminator can recognize coarse to fine image features, thereby guiding the generator to produce more realistic results. Each individual discriminator employs the architecture of the PATCHGAN discriminator [45], which penalizes only the structure at the scale of patches; in other words, the final output of the discriminator is not a value but a matrix in which each value corresponds to a perceptual field with a specified size in the original graph. Accordingly, networks can devote attention to the structure in local image patches and model high-frequency details. Spectral normalization is implemented in each convolutional layer of the discriminator module in order to stabilize the training of the network by making the layers satisfy the Lipschitz constant [46].

III. EXPERIMENTAL RESULTS AND DISCUSSION

A. Dataset and parameter settings

In this part, we discuss experiments on three types of granular porous media, i.e., a bead pack with regular spherical grains, Fontainebleau sandstone with relatively rounded grains, and Belgian fieldstone with irregularly shaped grains, to validate the effectiveness of our approach.

Bead pack. The bead pack is an artificial core formed by a number of uniform spheres stacked at random [47]. The binary image consists of 500^3 voxels with a resolution of 3 μm, and each sphere has a diameter of 50 voxels.

Fontainebleau sandstone. As a kind of sedimentary rock resulting from the deposition of quartz grains followed by consolidation, Fontainebleau sandstone is an ideal granular system composed of monocrystalline quartz grains that have been well rounded during prolonged transportation before deposition [48,49]. This binary sample consists of 225^3 voxels with a resolution of 10 μm.

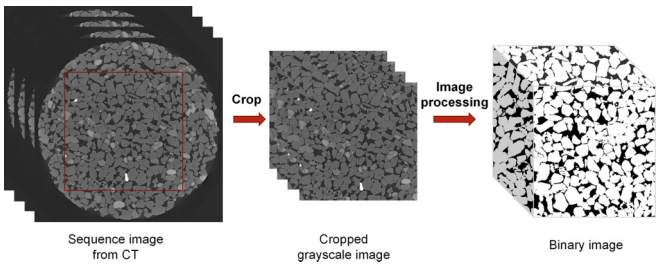

FIG. 5. Acquisition process of the binary 3D structure of the Belgian fieldstone. White represents grain phase, and black represents pore phase.

Belgian fieldstone. The Belgian fieldstone sample was acquired with the HECTOR micro-CT scanner with a 4 mm diameter and is a type of sandstone rich in glauconite [50]. The Belgian fieldstone consists of many irregularly shaped grains with sharp angles, most of which adhere together without obvious borders. Grayscale 2D slice images extracted from the original CT sequence images for a region of interest are displayed in Fig. 5. As our attention is focused on two-phase 3D reconstruction in this paper, the grayscale image was separated into two phases: pore and grain.

The datasets for training are obtained by means of cropping out images of a specific size from the associated original 3D structure in a certain step. Moreover, it is noteworthy that the extracted subvolumes should be larger than the representative elementary volume (REV) because the REV is the minimum unit which can effectively characterize physical properties of porous media [51]. As a result, the original 3D structure is sometimes downsampled before being cropped to meet requirements when creating a dataset.

Because hyperparameters influence the performance of the model to some extent, we list the determined settings for the hyperparameters in the experiments after several trials in Table I. In our study, all experiments were conducted on a desktop with an i7-9700 CPU and NVIDIA GeForce RTX 2080 Ti GPU.

B. Evaluation criteria

In this section, we describe in detail the evaluation criteria for reconstruction in this paper from statistical and morphological points of view.

1. The autocorrelation function

The autocorrelation function (ACF) is used to quantify the spatial correlation of two points in the structure with an indicator function $I(\mathbf{x})$ which describes the probability that two random points with a separation $r = \|\mathbf{r}\|$ belong to the same phase:

$$I(\mathbf{x}) = \begin{cases} 1, & \mathbf{x} \in \text{grain}, \\ 0, & \mathbf{x} \notin \text{grain}, \end{cases} \tag{11}$$

where $\mathbf{x}$ denotes the position in the medium. The formula for the ACF is given by

$$\mathcal{R}(\mathbf{r}) = \frac{\langle [I(\mathbf{x}) - \phi][I(\mathbf{x}+\mathbf{r}) - \phi] \rangle}{\phi - \phi^2}, \tag{12}$$

where ϕ indicates the volume fraction of the grain phase.

2. Multiple-point connectivity

As the autocorrelation function previously described can characterize only the relationship between two points, multiple-point connectivity (MPC) is imported to describe higher-order information about the image data. MPC can measure the spatial connectivity in the grain phase by means of calculating the probability that a certain number of continuous points along a given direction lie entirely in the same phase of interest, which can be calculated as

$$\begin{aligned} F(\mathbf{h}; n) &= \mathbb{E}\{I(\mathbf{x}) \cdot I(\mathbf{x}+\mathbf{h}) \cdot \cdots \cdot I[\mathbf{x} + (n-1)\mathbf{h}]\} \\ &= \mathbb{E}\left\{ \left(\prod_{j=0}^{n-1} I(\mathbf{x} + j\mathbf{h}) \right) \right\}, \end{aligned} \tag{13}$$

where $\mathbf{h}$ is a directionally determined unit vector and n is the number of points involved in each calculation.

3. Grain morphology descriptors

The granular images, including the real samples and the generated ones, were processed using AVIZO software [52] with respect to grain attributes.

In general, the morphological parameters of grain are as described below. The primary focus of our analysis is three-dimensional grains.

Area3d. Area3d is the surface area of a grain in three-dimensional space which is denoted as A_{3d}.

TABLE I. Network configurations and hyperparameters.

	Training image dataset		
Parameters	Bead pack	Fontainebleau sandstone	Belgian fieldstone
Training image size	128^3 voxels	128^3 voxels	128^3 voxels
Size of the latent vector	128	128	128
Size of the noise latent vector	32	32	32
Encoder and generator filters	32	32	32
discriminator filters	16	16	16
Learning rate	4×10^{-4}	4×10^{-4}	4×10^{-4}
Dilation rate	4	2	2
Loss weights λ_{kl}, λ_{rec}, λ_{gan}, λ_{pattern}	0.1, 10, 0.1, 1×10^6	0.1, 10, 0.1, 1×10^6	0.1, 10, 0.1, 1×10^6

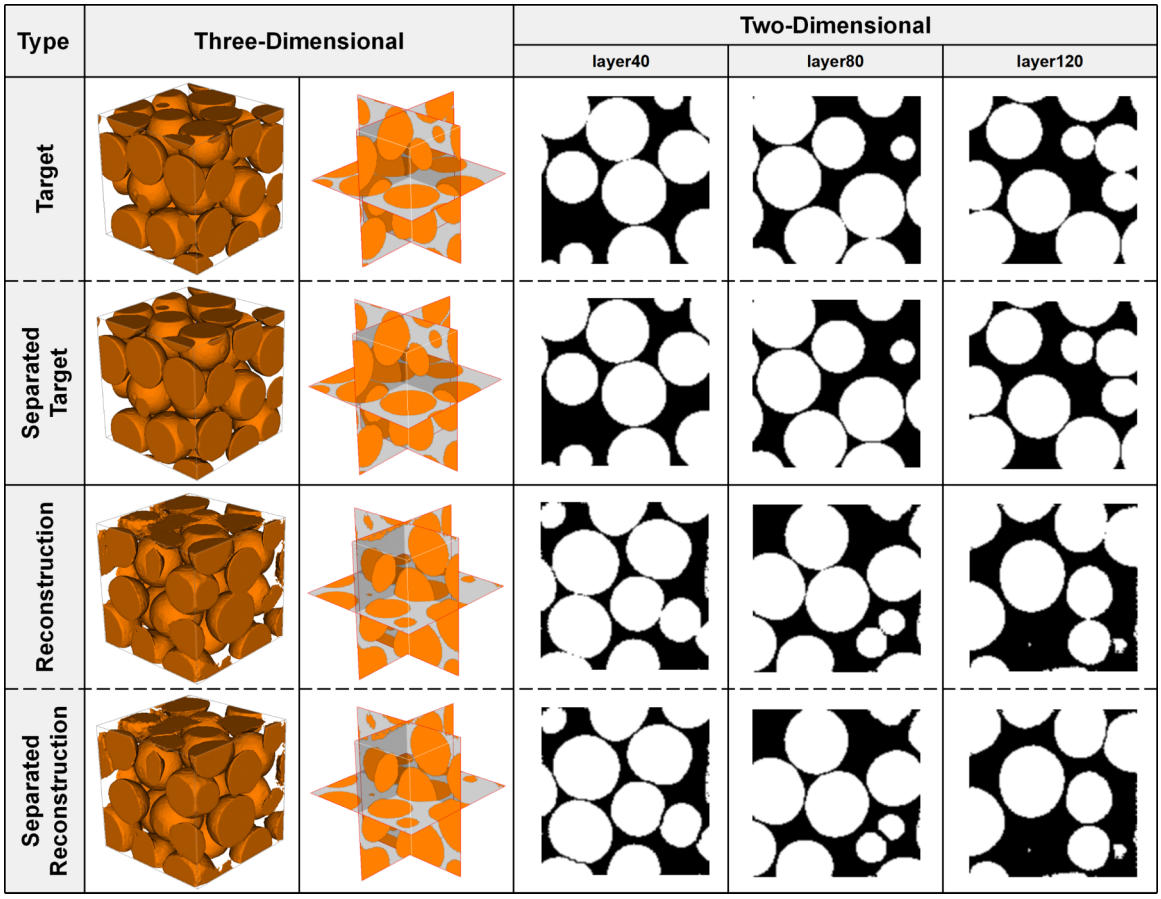

FIG. 6. Visual presentation of target and reconstruction samples of the bead pack and their corresponding split versions. The "Two-Dimensional" section displays 2D slice images at layer 40, layer 80, and layer 120.

Volume3d. Volume3d is the volume of a grain in three-dimensional space which is denoted as V_{3d}.

Grain size. For a given grain, the equivalent diameter (denoted as D_e) is obtained by taking the diameter of an equivalent spherical grain with the same volume as the given irregularly shaped grain. So the grain size is given by the following expression:

$$D_e = \sqrt[3]{\frac{6 \times V_{3d}}{\pi}}. \tag{14}$$

Sphericity. Sphericity is a measure of the degree to which a grain approaches the shape of a perfect sphere. Sphericity, denoted as Ψ, is defined as the ratio of the surface area of a sphere S_{sphere} with the same volume as the given grain to that of the grain itself S_{grain} [53] as Eq. (15) shows. Owing to the isoperimetric inequality, the sphericity of grains is bounded by 1. Nonetheless, it is worth noting that the sphericity computed in the study could be superior to 1 for certain small grains, whereas the surface area of the grain is computed with chordal approximations:

$$\Psi = \frac{S_{\text{sphere}}}{S_{\text{grain}}} = \frac{\pi^{1/3} \times (6 \times V_{3d})^{2/3}}{A_{3d}}. \tag{15}$$

Elongation and flatness. As two form ratios, flatness index (FI) and the elongation index (EI) [54] are quantifications of the degree of grain flattening and grain elongation, respectively. As symbols a, b, and c represent length, thickness, and breadth with length, respectively, FI and EI can be expressed as c/b and b/a.

C. Results and comparisons

In this part, we elucidate the reconstruction performance of our method in the experiments conducted on three datasets with significant differences in shape. To substantiate the effectiveness of our approach, both visual and quantitative comparisons are displayed.

1. Bead pack reconstruction

First, we present experiments on bead pack samples stacked by regular spherical grains whose visual presentation is shown in the "Target" row of Fig. 6. We pick the bottom 2D image of the target 3D structure as the input to the network and generate 10 stochastic reconstructions for quantitative analysis of statistical and morphological characteristics, one of which is depicted in Fig. 6. In addition, with the aim of identifying features of individual grains, we utilize the AVIZO software to segment adhesive grains, and Fig. 6 shows the corresponding results. Meanwhile, parameter analyses of the pore network are also conducted in order to further validate the effectiveness of our method. Specifically, we utilize the

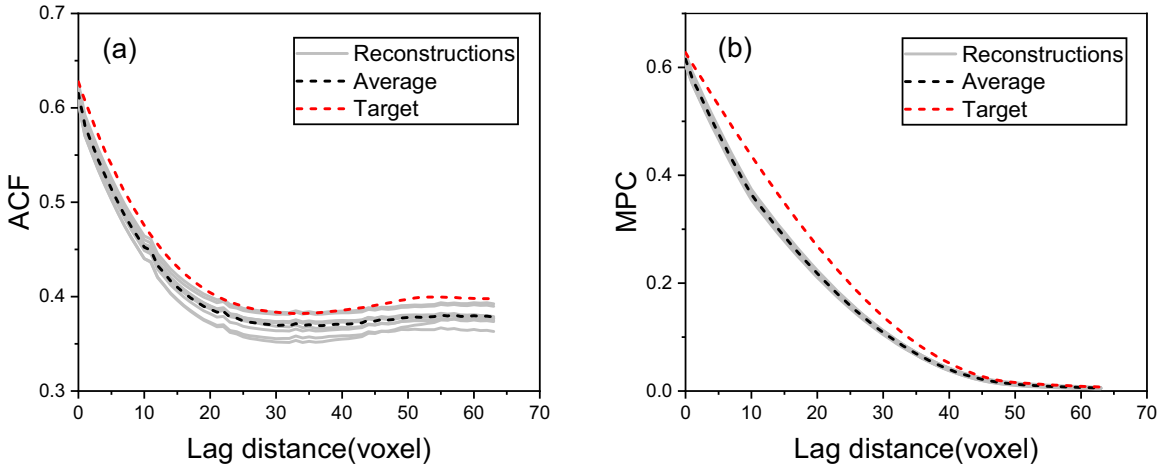

FIG. 7. Comparison of the average (a) the ACF and (b) MPC in the X, Y, and Z directions among the target, 10 reconstructions, and their average.

network extraction technique introduced by Dong and Blunt [49] to quantify the morphological characteristics of pores which enables the extraction of the parametric geometry and interconnectivity by simplifying the topologically disordered pore and throat network. The distribution and volume of the pores, along with the size and distribution of the throat connecting the pores, are the primary factors influencing the storage and transport properties of the microstructure. The morphology of the pores is directly associated with the shape factor. The pore connectivity is revealed by the coordination number and permeability. In addition, we calculate the tortuosity [55] using the AVIZO software and Euler number [56] with PYTHON library functions to obtain the topology properties of the pore space.

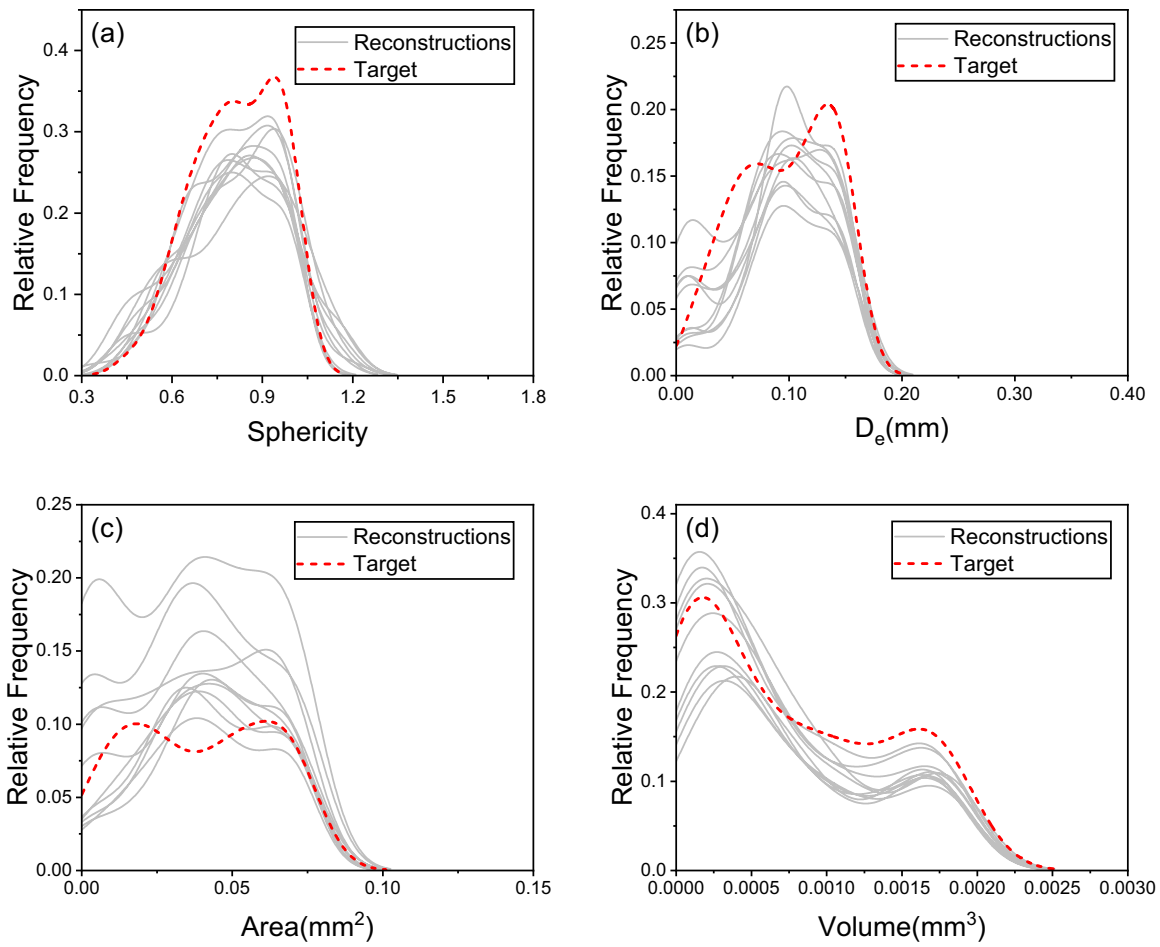

FIG. 8. Comparison of (a) the sphericity, (b) D_e, (c) surface area, and (d) volume of grains in the target and 10 reconstructions.

TABLE II. Comparison of morphological parameters of the grain and pore in the bead pack.

Parameters	Target	Reconstruction	Relative errors
Number of grains	49	51	4.08%
Volume fraction of grain phase	0.6275	0.6154	1.93%
Average sphericity of grains	0.8147	0.8118	0.35%
Average EI of grains	0.7845	0.7081	9.74%
Average FI of grains	0.4155	0.4164	0.22%
Average D_e of grains (mm)	9.683×10^{-2}	9.364×10^{-2}	3.30%
Average surface area of grains (mm^2)	3.907×10^{-2}	3.955×10^{-2}	1.23%
Average volume of grains (mm^3)	7.219×10^{-4}	6.843×10^{-4}	5.21%
Number of pores	39	58	47.69%
Number of throats	127	211	66.30%
Average shape factor of pores	0.0290	0.0289	0.43%
Average size of pore radius (mm)	2.130×10^{-2}	1.992×10^{-2}	6.50%
Average size of throat radius (mm)	9.661×10^{-3}	8.772×10^{-3}	9.72%
Average volume of pores (mm^3)	4.942×10^{-4}	3.483×10^{-4}	29.53%
Average volume of throats (mm^3)	13.51×10^{-6}	8.269×10^{-6}	38.80%
Average ratio of the radius size of the pore and throat	0.3182	0.3136	1.46%
Average coordination number	6.564	7.373	12.32%
Euler number of the pore phase	−52	−51	1.92%
Tortuosity	1.338	1.388	3.74%
Absolute permeability (m^2)	1.005×10^{-11}	1.317×10^{-11}	31.08%

From a visual point of view, the realization is highly consistent with the real sample in terms of geometrical morphology, except that not all the grains in the realization are perfectly regular spheres, in contrast to the real sample, and some are close to ellipsoids. As seen in Fig. 7, comparisons of the average autocorrelation function and multipoint connectivity

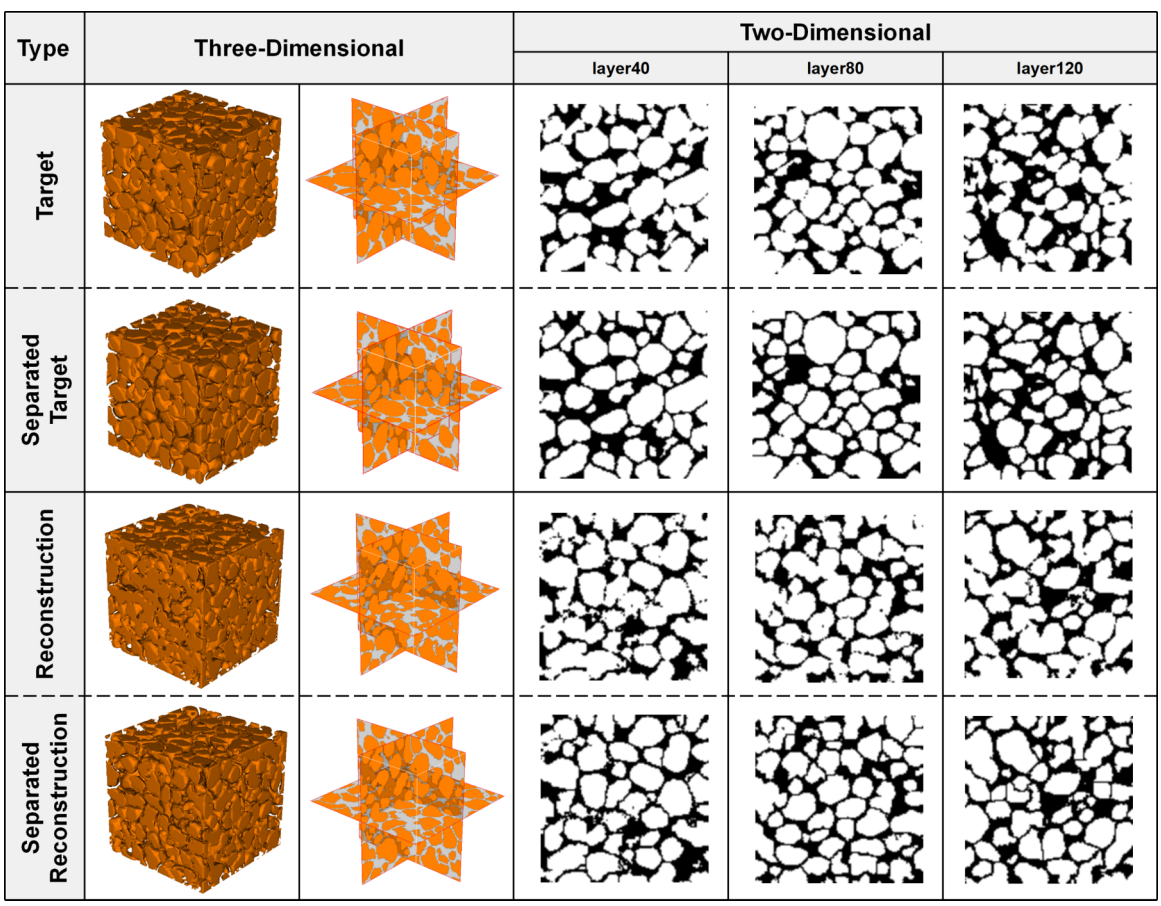

FIG. 9. Visual inspection of the target and reconstruction samples of the Fontainebleau sandstone and their corresponding split versions. The "Two-Dimensional" section displays 2D slice images at layer 40, layer 80, and layer 120.

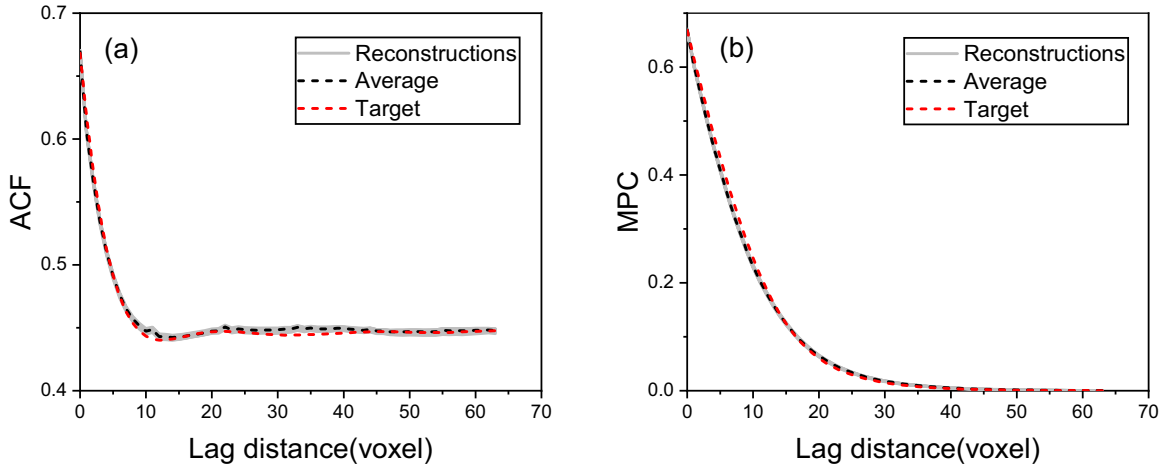

FIG. 10. Comparison of the average (a) the ACF and (b) MPC in the X, Y, and Z directions among the target, 10 reconstructions, and their average.

in the X, Y, and Z directions among the target, 10 reconstructions, and their average indicate that, by and large, the generated results agree well with the target in the aspect of statistical features. Not only that, but we also quantitatively analyze the morphological characteristics of grains, as shown in Fig. 8, which demonstrates the closeness between the respective distributions of four descriptors of grains in the realizations and the target. Notably, the relative frequency of small sizes in the distribution of the equivalent diameter, surface area, and volume of grains in realizations is higher than in the real sample due to the presence of some undesired isolated small structures in the generated results. Some

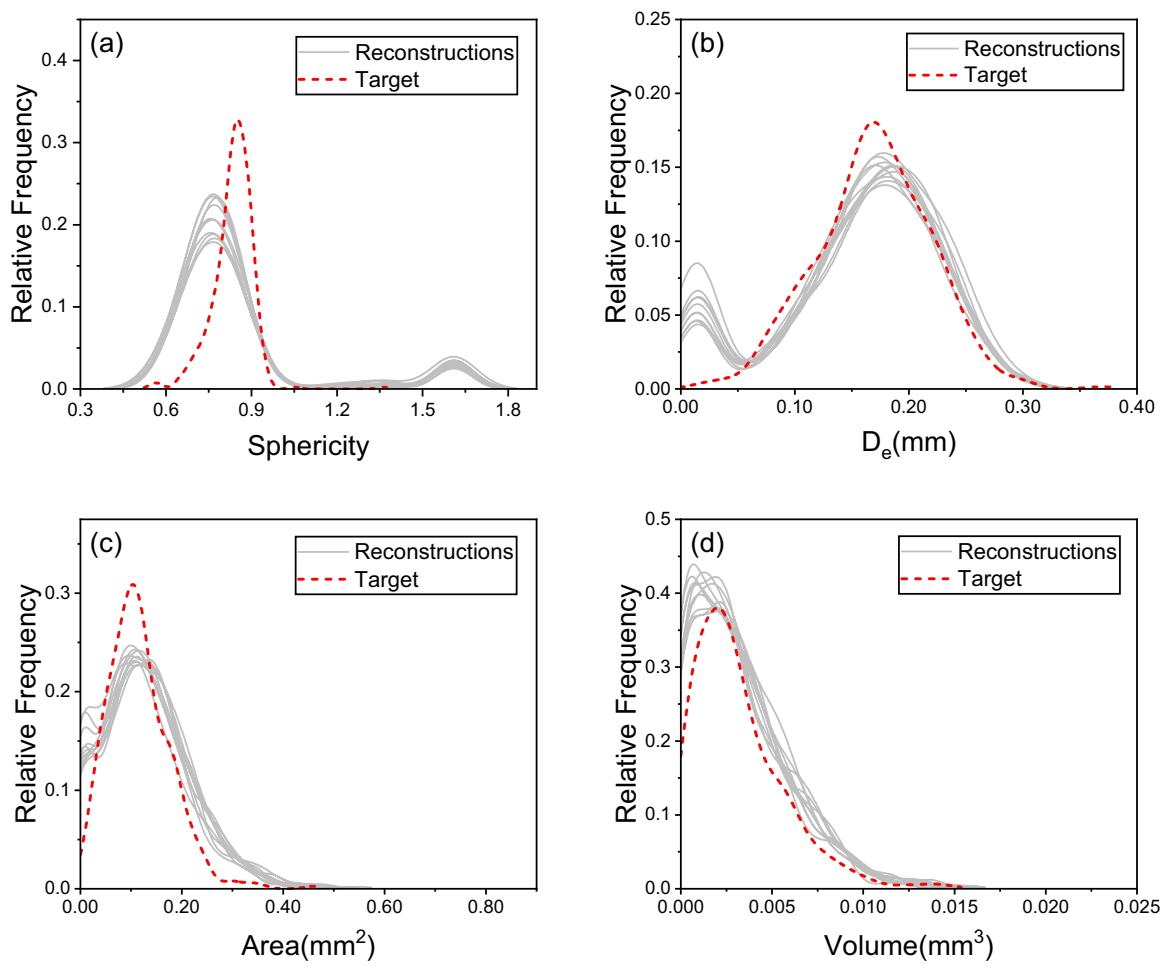

FIG. 11. Comparison of (a) the sphericity, (b) D_e, (c) surface area, and (d) volume of grains in the target and 10 reconstructions.

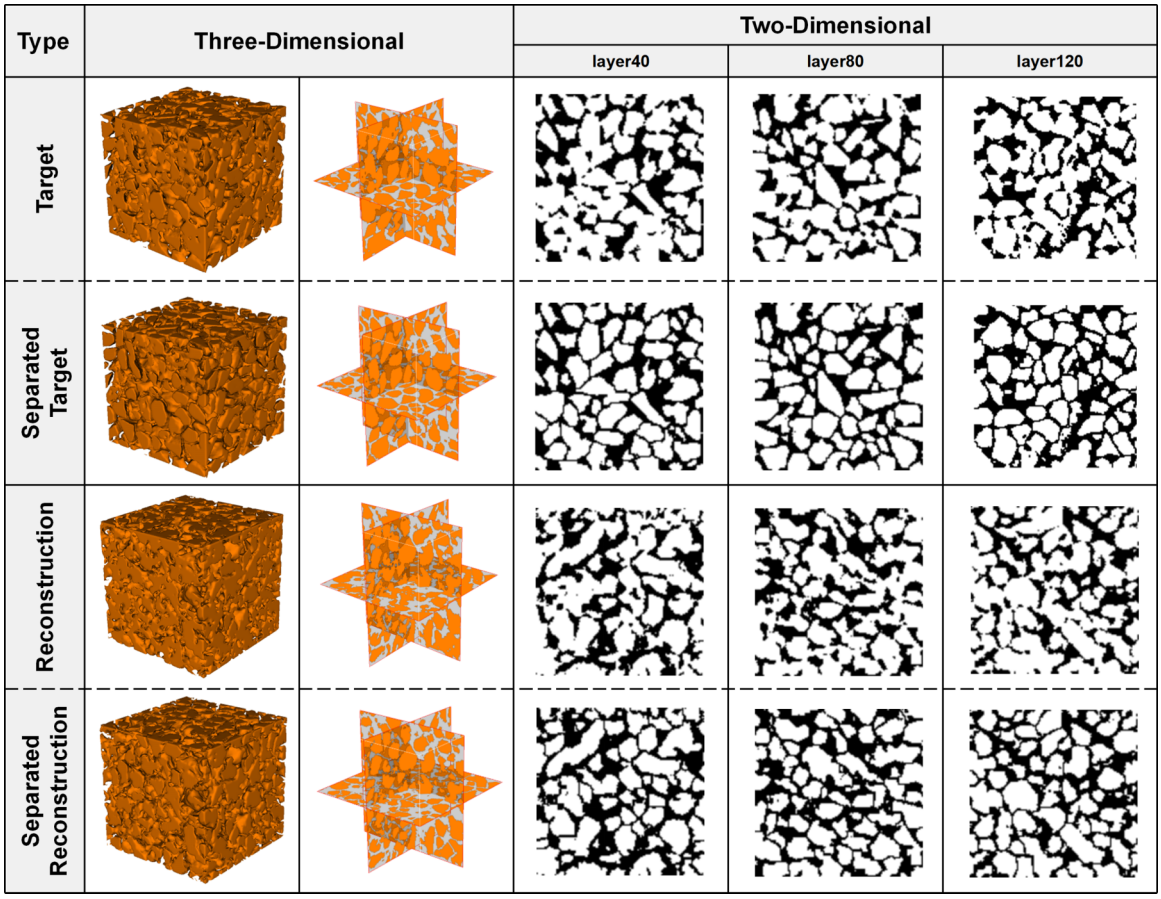

FIG. 12. Visual inspection of the target and reconstruction samples of the Belgian fieldstone and their corresponding split versions. The "Two-Dimensional" section displays 2D slice images at layer 40, layer, 80 and layer 120

important parameters of the granular porous media are calculated and listed in Table II. The relative errors of the parameters related to grains are no more than 10%, and the majority of parameters with regard to the pores in the reconstructions exhibit good consistency with those of the target, with only a few exceptions. It should be pointed out that the substantial differences observed in the number of pores and throats, as well as the average volume of pores and throats, between the reconstructions and the target are likely attributed to the presence of undesired noise and incorrect segmentation in the pore space. Finally, it is worth noting that the model, once trained, takes only about 0.13 s for a 3D reconstruction when running on a desktop with an NVIDIA GeForce RTX 2080 Ti GPU. To sum up, our approach demonstrates high accuracy and efficiency in reconstructing structurally simple media.

2. Fontainebleau sandstone reconstruction

Because the bead pack manifests a simple granular porous media consisting solely of uniformly sized spherical components, we next take Fontainebleau sandstone with a comparatively rounded structure as the experimental object. The 3D structure and 2D slice images are illustrated in Fig. 9. Likewise, we generate 10 synthetic results for one input image to verify the applicability of our method for this type of medium. Comparisons including visual aspects and statistical and morphological features are carried out between generations and the target for a comprehensive analysis.

Figure 9 suggests that the realization of our model is composed of grains with a fairly rounded shape, which is in good agreement with the actual sample. From the perspective of statistical properties, the ACF and MCP curves of the target and the average of the generated results (see Fig. 10) almost exactly coincide. Additionally, the volume fraction of the grain phase accounts for a mere 0.16% relative error, and those of the target and the average of reconstructions are 0.6683 and 0.6693, respectively, which indicates the remarkably high accuracy attained through the proposed approach. Furthermore, comparisons of the morphological parameters of the grains are conducted to evaluate the reconstruction ability of the model and are shown in Fig. 11 and Table III. As can be seen from the data in Table III, the relative errors of the calculated parameters are basically in the range of 0.1%−7.0%, whereas the average of the FI and surface area of the grains in reconstructions are a bit different from those of the target. The pore network of the structures is also analyzed and presented in Table III. The small relative error, particularly within 1.0% for the average shape factor and tortuosity, demonstrates the excellent accuracy of our reconstruction method. As illustrated in Fig. 11, although the general trend of the distribution curves is consistent, there are more small-sized grains in the reconstructions than in the target. This

TABLE III. Comparison of morphological parameters of the grain and pore in Fontainebleau sandstone.

Parameters	Target	Reconstruction	Relative errors
Number of grains	421	423	0.48%
Volume fraction of grain phase	0.6683	0.6693	0.16%
Average sphericity of grains	0.8341	0.8495	1.85%
Average EI of grains	0.5462	0.5128	6.12%
Average FI of grains	0.5089	0.5515	8.37%
Average D_e of grains (mm)	0.1693	0.1576	6.88%
Average surface area of grains (mm^2)	0.1160	0.1256	8.35%
Average volume of grains (mm^3)	3.213×10^{-3}	3.133×10^{-3}	2.48%
Number of pores	591	699	18.27%
Number of throats	2279	2571	12.80%
Average shape factor of pores	0.0295	0.0295	0.00%
Average size of pore radius (mm)	2.538×10^{-2}	2.260×10^{-2}	10.95%
Average size of throat radius (mm)	10.15×10^{-3}	9.242×10^{-3}	8.91%
Average volume of pores (mm^3)	10.37×10^{-4}	8.784×10^{-4}	15.26%
Average volume of throats (mm^3)	3.638×10^{-5}	3.121×10^{-5}	14.23%
Average ratio of the radius size of the pore and throat	0.2982	0.2903	2.63%
Average coordination number	7.716	7.358	4.63%
Euler number of pore phase	−1118	−1277	14.22%
Tortuosity	1.497	1.506	0.57%
Absolute permeability (m^2)	8.520×10^{-12}	7.454×10^{-12}	12.51%

issue will be further discussed and improved in our future work.

3. Belgian fieldstone reconstruction

The demand for a more quantitatively reliable model persists as a result of naturally occurring grains with irregular and angular shapes in granular porous media. Finally, we perform a reconstruction experiment on Belgian fieldstone with a more complicated structure than the two samples discussed previously. Figure 12 depicts one example of such images and the corresponding generated realizations, as well as the respective versions of grains being separated. In addition, the statistical and morphological features of the 3D structure are quantitatively evaluated (see Figs. 13 and 14).

Visually speaking, the 3D complex topology of the grains has been comparatively well restored, illustrating the capability of our approach to reconstruct a 3D structure with a similar spatial distribution of grains by thoroughly considering and leveraging the extracted feature information. With respect to the statistical information shown in Fig. 13, the results generated by our method are in good agreement with the real sample. Figure 14 indicates that the overall trend of the distribution curves is consistent between the reconstructions and the target, although some differences in the details do exist. As can be seen from Fig. 14(a), the results generated by our method comprise more irregularly shaped grains, which is consistent with the visual presentation in Fig. 9. Figures 14(b) and 14(d) suggest that, in spite of the similar volume distributions, the reconstructed results have a

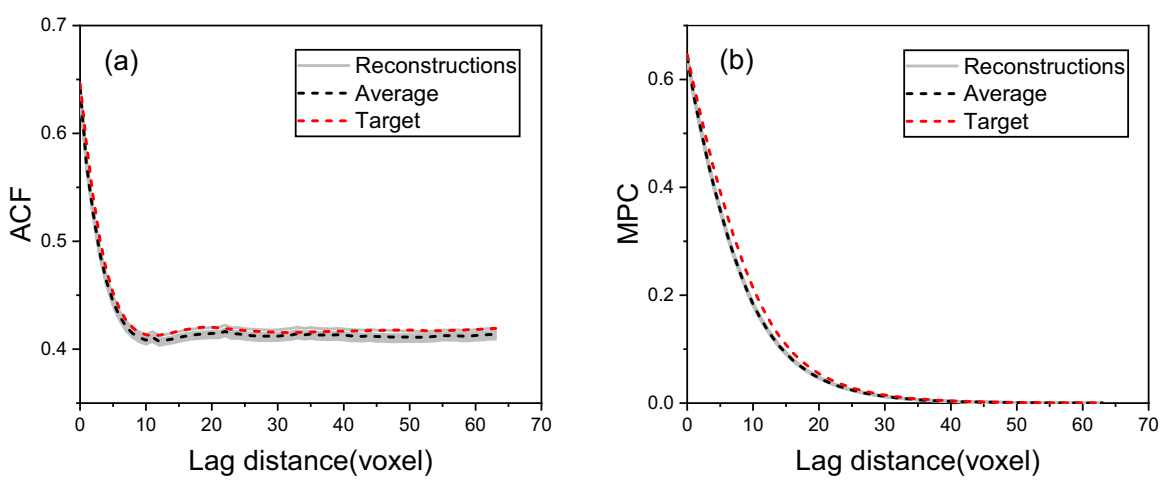

FIG. 13. Comparison of the average (a) the ACF and (b) MPC in the X, Y, and Z directions among the target, 10 reconstructions, and their average.

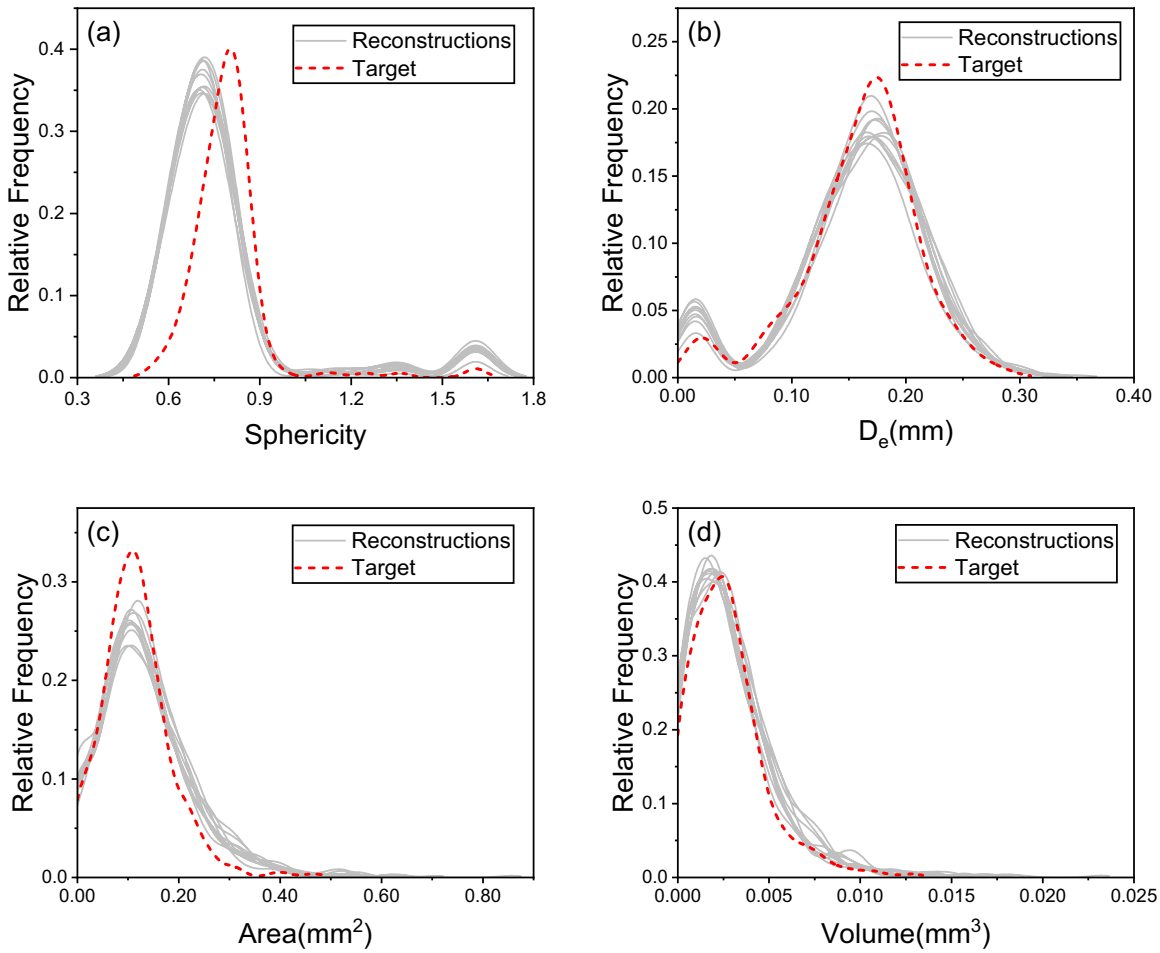

FIG. 14. Comparison of (a) the sphericity, (b) D_e, (c) surface area, and (d) volume of granules in the target and 10 reconstructions.

TABLE IV. Comparison of morphological parameters of the grain and pore in Belgian fieldstone.

Parameters	Target	Reconstruction	Relative errors
Number of grains	501	469	6.39%
Volume fraction of the grain phase	0.6463	0.6418	0.70%
Average sphericity of grains	0.7959	0.7698	3.29%
Average EI of grains	0.5255	0.4866	7.40%
Average FI of grains	0.4968	0.5349	7.67%
Average D_e of grains (mm)	0.1597	0.1576	1.27%
Average surface area of grains (mm^2)	0.1166	0.1278	9.61%
Average volume of grains (mm^3)	2.747×10^{-3}	2.872×10^{-3}	4.57%
Number of pores	835	981	17.49%
Number of throats	3069	3607	17.53%
Average shape factor of pores	0.0298	0.0287	0.45%
Average size of the pore radius (mm)	2.303×10^{-2}	2.152×10^{-2}	6.55%
Average size of the throat radius (mm)	9.702×10^{-3}	8.933×10^{-3}	7.92%
Average volume of pores (mm^3)	8.449×10^{-4}	7.374×10^{-4}	12.73%
Average volume of throats (mm^3)	3.074×10^{-5}	2.434×10^{-5}	20.82%
Average ratio of the radius size of the pore and throat	0.3059	0.2947	3.67%
Average coordination number	7.353	7.358	0.07%
Euler number of the pore phase	−2401	−3130	30.36%
Tortuosity	1.538	1.507	1.99%
Absolute permeability (m^2)	7.882×10^{-12}	6.611×10^{-12}	16.13%

TABLE V. Euler number and three associated Betti numbers.

	Bead pack		Fontainebleau sandstone		Belgian fieldstone	
Parameters	Target	Reconstruction	Target	Reconstruction	Target	Reconstruction
Euler number of the pore phase	−52	−51	−1118	−1277	−2401	−3130
Zeroth Betti number β_0	1	21	33	102	208	213
First Betti number β_1	61	94	1160	1405	2688	3524
Second Betti number β_2	8	22	9	26	79	181

higher relative frequency of D_e at small sizes than the real 3D image. A comparison of the morphological parameters of the grain and pore in Belgian fieldstone are given in Table. IV. It is noteworthy that, despite our main focus on grain reconstruction in the media system, the parameters of the pores in the generated results align well with those of the actual sample.

D. Discussion

This paper presents a method for three-dimensional reconstruction of the granular porous media based on deep generative models. In Sec. III C, the results and comparisons conducted for three different types of samples with varying grains demonstrate that, overall, the important parameters related to the grain and pore exhibit good agreement with the ground truth. In addition, due to our focus on grains, the relative errors of grain-related parameters are generally smaller than those of pore-related parameters.

In previous comparisons, our reconstructed results performed well in terms of morphological parameters but slightly worse in terms of the topological structure parameters such as the Euler number. Sometimes two systems may have the same Euler characteristic, but their topological structures can differ significantly. Therefore, to further validate the ability of our method to reproduce the topological structure of pore networks, we introduce Betti numbers, which are topological invariants. Their relationship with the Euler characteristic is shown by the following formula:

$$\chi = \beta_0 - \beta_1 + \beta_2, \tag{16}$$

where β_0 is the zeroth Betti number, β_1 is the first Betti number, and β_2 is the second Betti number. The three Betti numbers describe the number of isolated objects, tunnels, and cavities, respectively.

Since the Euler characteristic can be regarded as a linear combination of Betti numbers, the utilization of Betti numbers enables the provision of more comprehensive and detailed information about the topology [57]. Hence, we additionally calculate and compare the Betti numbers for all three sets of samples, and the corresponding results are presented in Table V. The findings reveal that the reconstructed samples exhibit a higher number of isolated connected components, tunnels, and enclosed solid cavities within the pore space.

TABLE VI. Comparison of the morphological parameters of the grain and pore in the bead pack before and after denoising.

Parameters	Target	Reconstruction	Relative error	Denoised results	Relative error
Number of grains	49	51	4.08%	46	6.12%
Volume fraction of grain phase	0.6275	0.6154	1.93%	0.6178	1.55%
Average sphericity of grains	0.8147	0.8118	0.35%	0.8060	1.07%
Average EI of grains	0.7845	0.7081	9.74%	0.7165	8.67%
Average FI of grains	0.4155	0.4164	0.22%	0.4498	8.26%
Average D_e of grains (mm)	9.683×10^{-2}	9.364×10^{-2}	3.30%	10.21×10^{-2}	5.44%
Average surface area of grains (mm^2)	3.907×10^{-2}	3.955×10^{-2}	1.23%	4.260×10^{-2}	9.04%
Average volume of grains (mm^3)	7.219×10^{-4}	6.843×10^{-4}	5.21%	7.573×10^{-4}	4.90%
Number of pores	39	58	47.69%	58	47.69%
Number of throats	127	211	66.30%	196	54.33%
Average shape factor of pores	0.0290	0.0289	0.43%	0.0292	0.69%
Average size of pore radius (mm)	2.130×10^{-2}	1.992×10^{-2}	6.50%	2.041×10^{-2}	4.18%
Average size of throat radius (mm)	9.661×10^{-3}	8.772×10^{-3}	9.72%	8.970×10^{-3}	7.15%
Average volume of pores (mm^3)	4.942×10^{-4}	3.483×10^{-4}	29.53%	3.373×10^{-4}	31.75%
Average volume of throats (mm^3)	13.51×10^{-6}	8.269×10^{-6}	38.80%	9.963×10^{-6}	26.25%
Average ratio of the radius size of the pore and throat	0.3182	0.3136	1.46%	0.3232	1.57%
Average coordination number	6.564	7.373	12.32%	6.793	3.49%
Euler number of the pore phase	−52	−51	1.92%	−57	9.62%
Zeroth Betti number β_0	1	21	2000.00%	2	100.00%
First Betti number β_1	61	94	54.09%	67	9.84%
Second Betti number β_2	8	22	175.00%	8	0.00%
Tortuosity	1.338	1.388	3.74%	1.461	9.19%
Absolute permeability (m^2)	1.005×10^{-11}	1.317×10^{-11}	31.08%	1.142×10^{-11}	13.63%

These differences indicate the limited capacity of our algorithm to accurately replicate the topological structure of pore networks in terms of Betti numbers. Drawing upon the previously calculated parameters, we determine the possible contributing factors for this performance could be small isolated connected components introduced by our method that can be considered unexpected noise, as well as the sensitivity of Betti numbers to noise. In order to validate our estimation, we select the bead pack sample set as an example and apply a specific threshold for denoising. Subsequently, we compute the parameters of the structure after eliminating the noise. The findings in Table VI suggest that with the removal of some small connected domains, most parameters exhibit minimal changes in accuracy. However, parameters such as the Betti number demonstrate a notable improvement in precision. Regarding how to optimize the algorithm to avoid excessive noise, identify an appropriate threshold selection strategy, and more accurately recover the topology of the pore networks, these will be the focal points of our future work.

IV. CONCLUSION

It is well known that accurate and fast generation of three-dimensional microstructures of granular porous media has been a long-standing challenge, especially when the data available for reference are scarce. To address this problem, a hybrid generative model incorporating the VAE and GAN was proposed to predict the entire 3D spatial distribution of the media from a single 2D slice image. A self-attention module was inserted in the network to better retrieve feature information, and pattern loss was added to the total loss function to enhance the quality of the synthesized structure. Our method treats the medium as a whole to account for the statistical properties of the overall system instead of treating simulated individual grains separately. The stochastically simulated 3D results for a specific type of granular porous medium from a single 2D image indicate good performance of the proposed approach from both visual impression and quantitative analysis. Furthermore, high-quality reconstructions obtained for three typical samples that each contained grains with unique morphologies demonstrated the good applicability of our method to different types of granular porous media. Another advantage of our method is that once the model has been trained, it takes only a few tenths of a second to rebuild a sample.

Although our method performs well in terms of reconstruction accuracy and efficiency, several limitations do need to be addressed in the future. For instance, the number of small-sized grains approximating noise is a bit too large, causing the distribution curve of the grain morphological parameters to be somewhat different from the real one. Moreover, the ability of the network to learn the morphological characteristics of granular porous media, especially those composed of complicated granules, is not yet strong enough, manifested by the variations in relation to the morphological parameters. In our future work, we will strive for an object function that can better characterize the geometry of granular porous media to constrain the network. In addition, the small isolated connected components introduced by our method may have a significant impact on some topological parameters such as Betti numbers. Optimizing algorithms to avoid excessive noise and accurately reproduce the topological structure of pore networks is also one of our future goals.

The data underlying this paper are available on request.

ACKNOWLEDGMENTS

This work was supported in part by the National Natural Science Foundation of China (Grant No. 62071315) and in part by the Natural Science Foundation of Sichuan Province (Grant No. 2022NSFSC0914).

[1] H. Deresiewicz, Adv. Appl. Mech. **5**, 233 (1958).
[2] P. Tahmasebi, M. Sahimi, and J. E. Andrade, Geophys. Res. Lett. **44**, 4738 (2017).
[3] F. N. Altuhafi, M. R. Coop, and V. N. Georgiannou, J. Geotech. Geoenviron. Eng. **142**, 04016071 (2016).
[4] X. Garcia, L. T. Akanji, M. J. Blunt, S. K. Matthai, and J. P. Latham, Phys. Rev. E **80**, 021304 (2009).
[5] P. N. Sen, Geophysics **49**, 586 (1984).
[6] K. S. Mendelson and M. H. Cohen, Geophysics **47**, 257 (1982).
[7] E. Rezaei, K. Zeinalzadeh, and B. Ghanbarian, J. Contam. Hydrol. **243**, 103918 (2021).
[8] W. Xu, K. Zhang, Y. Zhang, and J. Jiang, Water Resour. Res. **58**, e2021WR031433 (2022).
[9] R. Bostanabad, Y. Zhang, X. Li, T. Kearney, L. C. Brinson, D. W. Apley, W. K. Liu, and W. Chen, Prog. Mater. Sci. **95**, 1 (2018).
[10] H. Li, S. Singh, N. Chawla, and Y. Jiao, Mater. Charact. **140**, 265 (2018).
[11] Y. Wang, J.-Y. Arns, S. S. Rahman, and C. H. Arns, Phys. Rev. E **98**, 043310 (2018).
[12] B. Bera, S. K. Mitra, and D. Vick, Micron **42**, 412 (2011).
[13] P. Tahmasebi, F. Javadpour, and M. Sahimi, Transp. Porous Media **110**, 521 (2015).
[14] F. Archie, M. Z. Mughal, M. Sebastiani, E. Bemporad, and S. Zaefferer, Acta Mater. **150**, 327 (2018).
[15] G. Jin, T. W. Patzek, and D. B. Silin, in *SPE Western Regional/AAPG Pacific Section Joint Meeting, Long Beach, CA* (OnePetro, 2003), Paper No. SPE-83587-MS.
[16] P.-E. Øren and S. Bakke, Transp. Porous Media **46**, 311 (2002).
[17] W. Zhu, W. Yu, and Y. Chen, J. Appl. Geophys. **85**, 37 (2012).
[18] L. Vu-Quoc, X. Zhang, and O. Walton, Comput. Methods Appl. Mech. Eng. **187**, 483 (2000).
[19] F. V. Donzé, V. Richefeu, and S.-A. Magnier, Electron. J. Geotech. Eng. **8**, 44 (2009).
[20] A. A. Bandeira and T. I. Zohdi, Comput. Part. Mech. **6**, 97 (2019).
[21] L. Wang, R. Li, B. Wu, Z. Wu, and Z. Ding, Particuology **38**, 185 (2018).
[22] T. Mede, G. Chambon, P. Hagenmuller, and F. Nicot, Granular Matter **20**, 16 (2018).

[23] B. Nassauer, T. Liedke, and M. Kuna, Granular Matter **15**, 85 (2013).
[24] Y. Ju, Y. Huang, S. Su, J. Zheng, H. Xie, C. Chang, and F. Gao, Geomech. Geophys. Geo-Energy Geo-Resour. **4**, 327 (2018).
[25] P. Tahmasebi and M. Sahimi, Granular Matter **20**, 45 (2018).
[26] D. D. Chen, Q. Teng, X. He, Z. Xu, and Z. Li, Phys. Rev. E **89**, 013305 (2014).
[27] M. Gao, Q. Teng, X. He, C. Zuo, and Z. J. Li, Phys. Rev. E **93**, 012140 (2016).
[28] Y. Jiao, F. H. Stillinger, and S. Torquato, Phys. Rev. E **77**, 031135 (2008).
[29] M. L. Gao, X. H. He, Q. Z. Teng, C. Zuo, and D. D. Chen, Phys. Rev. E **91**, 013308 (2015).
[30] C. Zuo, Z. Pan, and H. Liang, Phys. Rev. E **97**, 033302 (2018).
[31] P. Tahmasebi and M. Sahimi, Phys. Rev. E **85**, 066709 (2012).
[32] G. Mariethoz and J. Caers, *Multiple-Point Geostatistics: Stochastic Modeling with Training Images* (Wiley, Hoboken, NJ, 2014).
[33] L. Mosser, O. Dubrule, and M. J. Blunt, Phys. Rev. E **96**, 043309 (2017).
[34] Y. Huang, Z. Xiang, and M. Qian, Phys. Rev. E **105**, 015308 (2022).
[35] F. Zhang, Q. Teng, H. Chen, X. He, and X. Dong, Comput. Mater. Sci. **186**, 110018 (2021).
[36] F. Zhang, X. He, Q. Teng, X. Wu, and X. Dong, J. Pet. Sci. Eng. **208**, 109652 (2022).
[37] J. Feng, X. He, Q. Teng, C. Ren, H. Chen, and Y. Li, Phys. Rev. E **100**, 033308 (2019).
[38] S. Kench and S. J. Cooper, Nat. Mach. Intell. **3**, 299 (2021).
[39] Y. Song, P. Ranjith, and B. Wu, Powder Technol. **392**, 424 (2021).
[40] T. Karras, S. Laine, and T. Aila, in *Proceedings of the IEEE/CVF Conference on Computer Vision and Pattern Recognition* (IEEE, Piscataway, NJ, 2019), pp. 4401–4410.
[41] D. P. Kingma and M. Welling, arXiv:1312.6114.
[42] I. J. Goodfellow, J. Pouget-Abadie, M. Mirza, B. Xu, D. Warde-Farley, S. Ozair, A. Courville, and Y. Bengio, Adv. Neural Inf. Process. Syst. **27** (2014).
[43] A. Radford, L. Metz, and S. Chintala, arXiv:1511.06434.
[44] A. Vaswani, N. Shazeer, N. Parmar, J. Uszkoreit, L. Jones, A. N. Gomez, Ł. Kaiser, and I. Polosukhin, Adv. Neural Inf. Process. Syst. **30** (2017).
[45] P. Isola, J.-Y. Zhu, T. Zhou, and A. A. Efros, in *Proceedings of the IEEE Conference on Computer Vision and Pattern Recognition* (IEEE, Piscataway, NJ, 2017), pp. 1125–1134.
[46] T. Miyato, T. Kataoka, M. Koyama, and Y. Yoshida, arXiv:1802.05957.
[47] J. Finney, Proc. R. Soc. London, Ser. A **319**, 479 (1970).
[48] D. A. Coker, S. Torquato, and J. H. Dunsmuir, J. Geophys. Res. **101**, 17497 (1996).
[49] H. Dong and M. J. Blunt, Phys. Rev. E **80**, 036307 (2009).
[50] W. De Boever, T. Bultreys, H. Derluyn, L. Van Hoorebeke, and V. Cnudde, Sci. Total Environ. **554–555**, 102 (2016).
[51] M. J. Blunt, *Multiphase Flow in Permeable Media: A Pore-Scale Perspective* (Cambridge University Press, Cambridge, 2017).
[52] Thermo Fisher Scientific, AVIZO software, version 9, Waltham, MA, 2018.
[53] H. Wadell, J. Geol. **40**, 443 (1932).
[54] T. Zingg, Beitrag zur schotteranalyse, Ph.D. thesis, ETH Zurich, 1935.
[55] S. J. Cooper, A. Bertei, P. R. Shearing, J. A. Kilner, and N. P. Brandon, SoftwareX **5**, 203 (2016).
[56] R. T. Armstrong, J. E. McClure, V. Robins, Z. Liu, C. H. Arns, S. Schlüter, and S. Berg, Transp. Porous Media **130**, 305 (2019).
[57] S. K. Giri and G. Mellema, Mon. Not. R. Astron. Soc. **505**, 1863 (2021).